Journal of
Applied Crystallography
ISSN 0021-8898

Received 26 September 2011
Accepted 18 January 2012

Single-pass flow-through reaction cell for high-temperature and high-pressure *in situ* neutron diffraction studies of hydrothermal crystallization processes

Fang Xia,[a,b] Joël Brugger,[a,b] Gujie Qian,[b,c] Yung Ngothai,[d] Brian O'Neill,[d] Jing Zhao,[b,d] Stewart Pullen,[e] Scott Olsen[e] and Allan Pring[a,b]*

[a]School of Earth and Environmental Sciences, University of Adelaide, North Terrace, Adelaide, South Australia, 5005, Australia, [b]Department of Mineralogy, South Australian Museum, North Terrace, Adelaide, South Australia, 5000, Australia, [c]Ian Wark Research Institute, University of South Australia, Mawson Lakes Campus, Mawson Lakes, South Australia, 5095, Australia, [d]School of Chemical Engineering, University of Adelaide, North Terrace, Adelaide, South Australia, 5005, Australia, and [e]The Bragg Institute, Australian Nuclear Science and Technology Organisation, Locked Bag 2001, Kirrawee DC, New South Wales, 2232, Australia. Correspondence e-mail: allan.pring@samuseum.sa.gov.au

A large-volume single-pass flow-through cell for *in situ* neutron diffraction investigation of hydrothermal crystallization processes is reported. The cell is much more versatile than previous designs owing to the ability to control independently and precisely temperature (up to 673 K), pressure (up to 46 MPa), flow rate (0.01–10 ml min^{-1}) and reaction-fluid volume ($\geq$65 ml). Such versatility is realized by an innovative design consisting of a room-temperature and ambient-pressure external fluid supply module, a high-pressure reaction module which includes a high-temperature sample compartment enclosed in a vacuum furnace, and a room-temperature and high-pressure backpressure regulation module for pressure control. The cell provides a new avenue for studying various parameters of hydrothermal crystallizations independently, *in situ* and in real time at extreme hydrothermal conditions (*e.g.* supercritical). The cell was successfully commissioned on the high-intensity powder diffractometer beamline, Wombat, at the Australian Nuclear Science and Technology Organisation by investigating the effect of pressure on the hydrothermal pseudomorphic conversion from $SrSO_4$ (celestine) to $SrCO_3$ (strontianite) at a constant temperature of 473 K and flow rate of 5 ml min^{-1}. The results show that the increase of pressure exerts a nonlinear effect on the conversion rate, which first increases with increasing pressure from 14 to 20 MPa, and then decreases when pressure further increases to 24 MPa.

1. Introduction

The mechanism and kinetics of hydrothermal crystallization processes are of great interest across a range of scientific disciples. For mineralogists and petrologists, a fundamental understanding of reaction mechanism and kinetics will lead to a clearer picture of the formation of minerals in crustal hydrothermal environments (Qian *et al.*, 2010); for hydrometallurgists, it will help optimize the physical and chemical reaction parameters for improved leaching and metal extraction (Ruiz *et al.*, 2011; Zhao *et al.*, 2010); and for materials chemists, it can be applied to guide the product-oriented design of conditions for the hydrothermal syntheses of novel technological materials, hence replacing the traditional time-consuming 'trial and error' practice (Francis & O'Hare, 1998; Davis & Lobo, 1992; Xia, Brugger, Ngothai *et al.*, 2009; Brugger, Mcfadden *et al.*, 2010). Unfortunately, the investigation of the crystallization mechanism and kinetics of hydrothermal processes remains challenging. The reasons for this are that, on one hand, hydrothermal reactions are complex processes involving a dynamic interplay between dissolution, formation of metastable intermediate phases, nucleation, crystal growth and mass transport (Brugger, Pring *et al.*, 2010), and on the other hand, *in situ* studies that are capable of providing valuable direct information about the reaction at elevated pressure and temperature have been rare owing to the limited availability of suitable scientific tools and experimental protocols.

In recent years, the scope for *in situ* direct observation of hydrothermal crystallizations has increased dramatically, thanks to the increasing availability of high-flux synchrotron

X-ray and neutron sources and the development of suitable hydrothermal cells (Evans *et al.*, 1995; Francis *et al.*, 1999; Walton & O'Hare, 2000; Ok *et al.*, 2010). Compared to X-ray diffraction, the neutron diffraction technique has the advantage that relatively large volumes of hydrothermal fluids and samples can be used (cm^3 *versus* mm^3 to μm^3), therefore enabling *in situ* investigations of crystallization under conditions close to those found in natural hydrothermal systems, and metallurgical leaching and materials syntheses on the laboratory and pilot scales. In addition, the weaker interaction of neutrons with the samples compared with X-rays limits the incidence of beam damage, which can strongly affect reaction kinetics and reaction products in synchrotron-based X-ray experiments (Mesu *et al.*, 2005). For these reasons, several hydrothermal cells have been developed for neutron diffraction, covering a wide range of temperature (up to 723 K), pressure (up to 35.5 MPa) and fluid volume (up to 320 ml), and have been applied in studies of mineral and novel materials crystallization (Walton *et al.*, 1999, 2000; Williams *et al.*, 2006; O'Neill *et al.*, 2006; Xia, Qian *et al.*, 2010; Xia, O'Neill *et al.*, 2010; Ok *et al.*, 2010). However, a hydrothermal reaction cell capable of operating over a wider range of hydrothermal conditions, combining features of independent and precise control of temperature, pressure, reaction-fluid volume and flow rate, has not been available. To remove these limitations, we have designed a single-pass flow-through cell, which has been commissioned at the high-intensity powder diffractometer (HIPD) beamline, Wombat, at the Australian Nuclear Science and Technology Organisation (ANSTO). The capability of the cell for *in situ* neutron diffraction of hydrothermal crystallization was demonstrated by a case study of the effect of pressure on the reaction kinetics of hydrothermal pseudomorphic conversion from $SrSO_4$ (celestine) to $SrCO_3$ (strontianite) at constant temperature and fluid flow rate.

2. Cell design

The design of the single-pass flow-through cell is illustrated in Fig. 1. The cell consists of three modules: a low-temperature (close to room temperature) and ambient-pressure external fluid supply module, a high-pressure reaction module which includes a high-temperature sample compartment enclosed in a vacuum furnace provided by ANSTO, and a room-temperature high-pressure backpressure regulation module. The external fluid supply and the high-pressure reaction modules are connected by a high-performance liquid chromatography (HPLC) pump and a backpressure regulator. In the following paragraphs, the principle of the cell operation will be explained, then the ANSTO vacuum furnace and three modules of the cell will be individually described, and finally the cell will be briefly compared with previous designs.

The cell design enables independent and accurate control of temperature, pressure and flow rate of the fluid. The reaction temperature is controlled by a vacuum furnace (item 8 in Fig. 1) provided by ANSTO. Apart from the sample compartment inside the vacuum furnace the rest of the cell is maintained at low temperatures (<323 K), as a result of efficient cooling achieved by the relatively long (3 m) travel path of the connecting tubing (item 4 in Fig. 1 or item 17 in Fig. 2), the relatively low fluid flow rate and the low thermal conductivity of 316-type stainless steel. The control of pressure is achieved by a combination of the HPLC pump (item 11

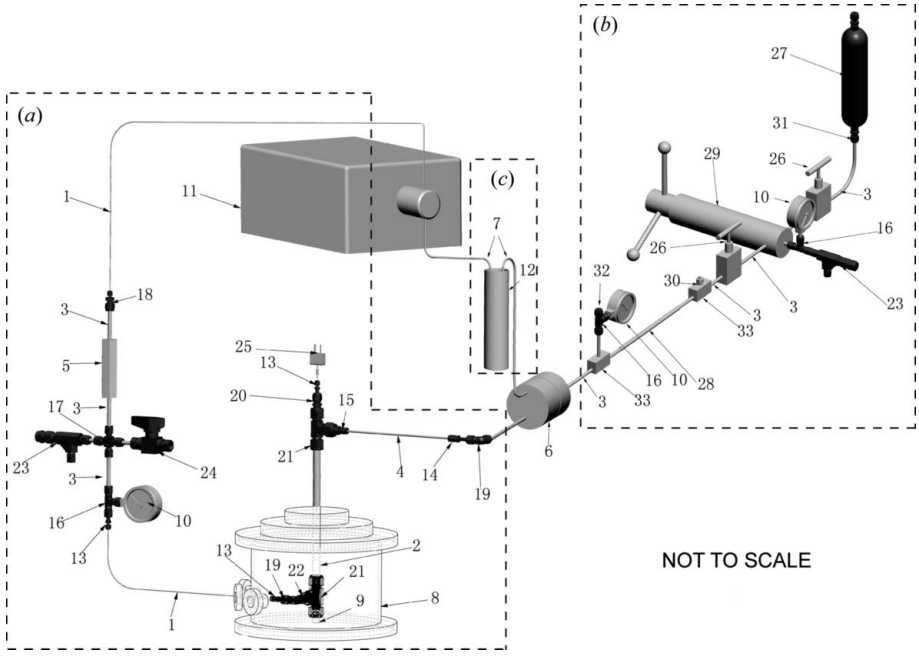

Figure 1
Schematic drawing of the single-pass flow-through cell. Three modules are shown in dashed borders: (*a*) the high-pressure reaction module; (*b*) the room-temperature high-pressure backpressure regulation module; and (*c*) the low-temperature (close to room temperature) and ambient-pressure external fluid supply module. (1) 1/16″ (1″ ≃ 2.54 cm) connecting tube (Swagelok); (2) 1/2″ sample compartment tube (Swagelok); (3) 1/4″ connecting tube (Swagelok); (4) 1/8″ connecting tube (Swagelok); (5) soft seat check valve (30-41HF4-T, HIP); (6) backpressure regulator (BP-100, Temco); (7) 1/4″ flexible silicone tubes; (8) vacuum furnace provided by ANSTO (vacuum pump and heater not shown); (9) custom made plug for centering; (10) pressure gauges (Swagelok, PGI-63B-LG25-LAOX, 0–25 MPa); (11) HPLC pump (Varian ProStar 210/218); (12) reaction solution bottle (500 ml); (13) reducer (Swagelok S-100-R-4); (14) reducer (Swagelok S-200-R-4); (15) reducer (Swagelok S-200-R-8); (16) 1/4″ union tee (Swagelok S-400-3); (17) 1/4″ union cross (Swagelok S-400-4); (18) reducing union (Swagelok S-400-6-1); (19) 1/4″ union elbow (Swagelok S-400-9); (20) reducer (Swagelok S-400-R-8); (21) 1/2″ union tee (Swagelok S-810-3); (22) reducing port connector (Swagelok S-811-PC-4); (23) pressure relief valve (Swagelok S-4R3A); (24) high-pressure ball valve (Swagelok S-83PS4); (25) K-type thermocouple; (26) needle valves (Nova Swiss 30-11H4F); (27) water reservoir (Swagelok 304 L-HDF4-300); (28) 10 m high-pressure flexible hose (Nova Swiss); (29) hand pump (Nova Swiss); (30) sealing plug (Nova Swiss PLG-20-4); (31) male connector (Swagelok S-400-1-4); (32) sealing plug (Swagelok S-400-P); (33) tees (Nova Swiss TEE-20-4M).

in Fig. 1) and the backpressure regulator (item 6 in Fig. 1). In operation, the reaction module is first filled with reaction fluid by priming the module using the HPLC pump; the HPLC pump delivers a constant flow rate, so the pressure within the reaction module is built up by increasing the pressure in the backpressure regulation module using a hydraulic hand pump (item 29 in Fig. 1); finally the pressure is increased to the target value, and is maintained steadily throughout the reaction both in the reaction and in the backpressure regulation modules. The fluid flow rate is controlled by the HPLC pump and can be precisely set in the range from 0.01 to 10 ml min^{-1}; higher rates are possible using different HPLC head assemblages, albeit at the cost of lowering the maximum working pressures.

The ANSTO vacuum furnace was designed to operate between room temperature and 723 K. The heating is applied *via* the use of three Heraeus shortwave IR lamps that deposit a combined 1.5 kW of IR power towards the sample compartment of the cell. The stray IR radiation is reflected back onto the sample using a parabolic mirror with the sample compartment at its focus. The IR lamps are controlled using a K-type thermocouple which provides feedback to a Eurotherm 3216 temperature controller. This in turn controls a Eurotherm TE10A thyristor which provides the appropriate duty cycling as applied by the controller. The vacuum furnace body is constructed using 6061-T6 aluminium with a thinned down section (2 mm) as a neutron window. The vessel was constructed to AS1210 pressure-vessel requirements and will operate at a vacuum of 1×10^{-5} mbar (1 mPa). The design provides two spare ports for the ability to flow fluid through the system and install additional sensors without affecting the integrity of the furnace. The maximum allowable temperature of the external furnace body is 373 K and this is maintained by heat sinking to the sample stage of Wombat. This customizable furnace had a lid produced especially for the purpose of the experiment and to cater for the various experimental setups that were required.

In the external fluid supply module, the reaction fluid is stored in a reservoir (item 12 in Fig. 1). The fluid is pumped from the reservoir by the HPLC pump through a flexible silicone hose and injected into the high-pressure reaction module *via* two check valves in the HPLC pump head (pressure rated to 60 MPa). After traveling through the reaction module, the fluid passes from the outlet of the backpressure regulator and returns to the same fluid reservoir (closed-loop mode) or to a second fluid reservoir (open mode) *via* another flexible silicone hose.

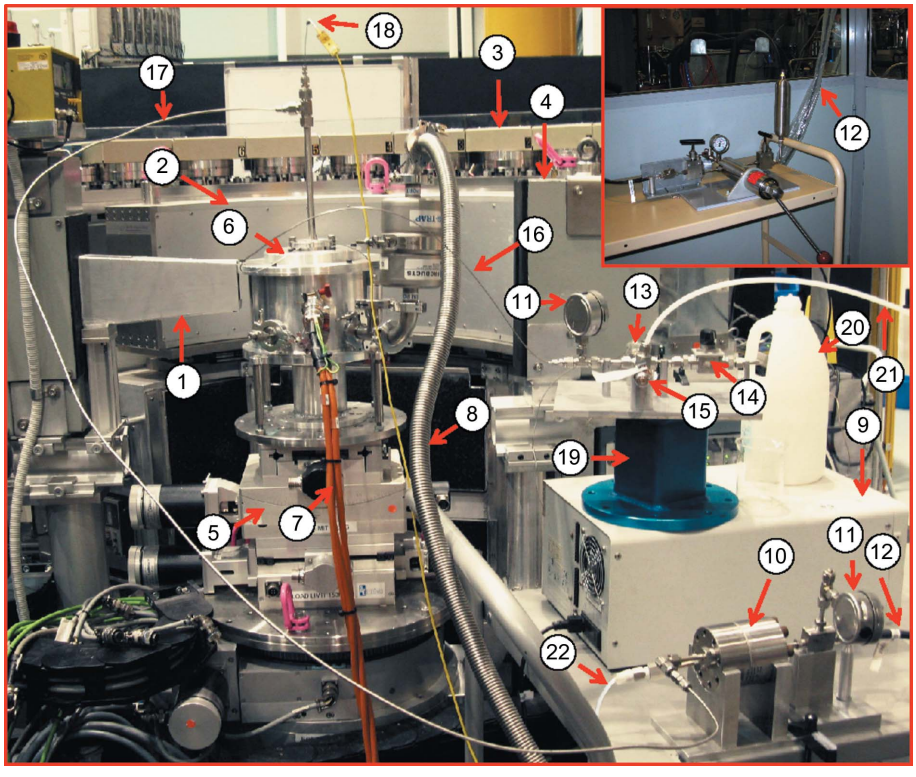

Figure 2
Setup of the hydrothermal cell on Wombat, the high-intensity powder diffractometer at ANSTO. (1) Neutron beam guide; (2) collimator; (3) detector; (4) beam stop; (5) four-dimensional adjustable stage; (6) ANSTO vacuum furnace; (7) power cable for the furnace; (8) vacuum tube; (9) HPLC pump; (10) backpressure regulator; (11) pressure gauges; (12) high-pressure flexible hose; (13) soft seat check valve; (14) ball valve for drainage; (15) pressure relief valve; (16) inlet tube of sample compartment; (17) outlet tube for sample compartment; (18) thermocouple; (19) positioning stage; (20) water reservoir for HPLC pump head cleaning; (21) drainage plastic tube for pressure relief; (22) outlet silicone tube of the backpressure regulator. The inset shows the hand pump for pressure generation and adjustment placed outside the instrument enclosure for remote control.

The reaction module has an internal volume of 65 ml and is composed of a series of Swagelok and HIP tubing and fittings. The reaction fluid is injected from the external fluid supply reservoir into this module by the HPLC pump. The fluid first travels through a soft seat check valve (item 5 in Fig. 1) to ensure the forward direction of the fluid flow, and then through the stainless steel sample compartment (item 2 in Fig. 1) sitting inside the ANSTO vacuum furnace, and finally flows through the backpressure regulator back to the external fluid supply module. Other components in this module include a cylinder-shaped sample tube made of 316-type stainless steel mesh (Locker Group, aperture diameter 47 µm) that is positioned in the center of the sample compartment, a pressure relief valve (item 23 in Fig. 1) to protect the system from pressure overshoot, a ball valve (item 24 in Fig. 1) for fluid drainage after the completion of the reaction, a pressure gauge (item 10 in Fig. 1) for monitoring system pressure, and a K-type thermocouple (item 25 in Fig. 1) with its measuring tip attaching to the mesh container for temperature recording at the sample position and also for sample loading (mesh sample container insertion) and extraction before and after the reaction. These

components are connected by Swagelok fittings (tubing, tee, reducer, elbow and cross) as illustrated in Fig. 1.

The backpressure regulation module consists of a Temco backpressure regulator (BP-100) connected to a hydraulic hand pump (item 29 in Fig. 1) *via* a 10 m high-pressure flexible hose. The temperature and pressure ratings for BP-100 are 394 K and 69 MPa, respectively. The water for the hydraulic pump is stored in a 300 ml reservoir (item 27 in Fig. 1). During pressurization of the backpressure regulation module, the pressure is monitored by two pressure gauges, one near the hand pump and the other near the backpressure regulator. A pressure relief valve (item 23 in Fig. 1) is installed near the hydraulic pump. Two valves are also fitted for initial water filling to the hand pump chamber and the high-pressure flexible hose from the water reservoir. The backpressure regulator operates based on a balanced-pressure principle. Once the process pressure at the outlet of the reaction module exceeds the dome pressure generated by the hydraulic hand pump, the Teflon diaphragm in the regulator flexes to allow the fluid to flow through, thus maintaining the process pressure. Once the process pressure drops below the dome pressure, the diaphragm will seal off the process and maintain the pressure.

In comparison with existing hydrothermal cells for *in situ* neutron diffraction, the current cell has several distinct features and advantages. (i) Unlike the previous cells in which pressures are temperature-dependent vapor-saturated values (Xia, Qian *et al.*, 2010; Xia, O'Neill *et al.*, 2010; O'Neill *et al.*, 2006; Ok *et al.*, 2010; Walton *et al.*, 1999), the temperature and pressure can be controlled independently in the new cell. This feature enables the study of the sole effect of temperature or pressure on the reaction kinetics of hydrothermal reactions *in situ*, which were not possible using previous cells. The independent effects of pressure or temperature are very important because for many hydrothermal reactions, such as those occurring deep in the Earth's crust, the reaction pressures are not vapor-saturated values. (ii) The current cell has higher temperature and pressure ratings. The temperature rating for the system is 673 K (determined by the ANSTO furnace). The pressure rating is determined by the mechanically weakest component in the system, the sample compartment. At room temperature, the wall-thickness-dependent pressure ratings of the sample compartment are 18, 35 and 46 MPa, for wall thicknesses of 0.89, 1.65 and 2.11 mm, respectively. These pressure ratings decrease with increasing temperature owing to the temperature-dependent tensile strength of stainless steel, by a factor of 0.96 at 473 K, 0.85 at 588 K and 0.80 at 673 K. Combined with independent control of pressure and temperature, these ratings enable the study of crystallization in aqueous systems under supercritical conditions *in situ* for a wide range of solvent properties (*e.g.* water density 0.11–0.56 g cm^{-3} at 673 K). (iii) The cell has the ability to rapidly heat the sample compartment to the target temperature. In our experiments, increasing the temperature from 293 to 473 K took only 4 min with a temperature overshoot of less than 3 K. Such rapid temperature increase minimizes the reaction extent below the target temperature, allowing for the collection of isothermal reaction kinetic data from very close to the beginnings of the hydrothermal reactions. The large improvement in heating rates is due to the fact that only a small portion (∼10 ml of fluid in the sample compartment) of the total reaction fluid (≥ 65 ml) needs to be heated. Once the fluid travels out of the sample compartment, it cools quickly to close to room temperature. In the previous cells, the entire fluid in the fluid reservoir (∼150 ml) needs to be heated up, which takes approximately 20 min before isothermal reaction data can be collected (Xia, Qian *et al.*, 2010; Xia, O'Neill *et al.*, 2010; O'Neill *et al.*, 2006). (iv) Because the external fluid supply module is operated at ambient temperature and pressure, the chemistry of the fluid can be easily controlled (*e.g.* controlled atmosphere) and the fluid volume can be extremely flexible. The fluid volume can be as small as the internal volume of the reaction module (∼65 ml) or as large as one wishes, allowing the setting of a wide range of solid to fluid ratios for hydrothermal crystallizations. (v) The separation of the fluid supply module from the reaction module allows the operation of the cell in either closed-loop mode or open mode, while previous cells can only operate in closed-loop mode. Open-loop operation mode enables continuous monitoring of solution parameters (*e.g.* Eh, pH, composition) both prior to and after the reaction, and opens the way for *in situ* study of mineral dissolution and crystallization under steady-state conditions, which is an important approach for getting theoretically meaningful rate constants (Nagy & Lasaga, 1992; Lasaga, 1998). (vi) The flow rate is independently controlled and can be finely tuned within the range 0.01–10 ml min^{-1}, while in previous cells the flow rate either is a fixed nonadjustable value owing to the use of a mechanical pump (O'Neill *et al.*, 2006) or is dependent on reaction temperature owing to the thermosyphon or convection principle of the fluid circulation (Xia, Qian *et al.*, 2010; Xia, O'Neill *et al.*, 2010). The precisely adjustable flow rate enables the investigation of the effects of flow rate on the reaction kinetics, more closely mimicking the conditions of particular hydrothermal crystallizations, such as mineral alterations deep in the Earth's crust.

3. Instrumental setup

The cell was commissioned on Australia's new HIPD beamline, Wombat, at ANSTO. The setup of the cell on Wombat is shown in Fig. 2. A neutron beam with a wavelength of 1.54 Å was selected using a vertically focusing germanium (115) monochromator at a takeoff angle of 90° (Studer *et al.*, 2006). The beam size was shaped by a slit system and in this study the size was 10 mm (width) × 40 mm (height) so as to completely immerse the central part of the sample compartment in the beam. After impinging on the sample, the neutrons first traveled through an oscillating radial collimator. The collimator eliminates unwanted background Bragg scattering, for example from the aluminium body of the vacuum furnace. Then the diffracted neutrons were detected by a 200 mm-high position-sensitive area detector spanning from 15 to 135° in 2θ. The distance from the sample to the front of the radial collimator was 430 mm, providing ample space for the ANSTO vacuum furnace. The 2θ position and the neutron wavelength

were calibrated using an alumina (Al_2O_3) standard. The intensities of the diffraction patterns were calibrated against the diffraction pattern of an empty vanadium can which is assumed to have uniform intensity in the two-dimensional detector.

4. Experimental test

The hydrothermal replacement reaction from $SrSO_4$ (the mineral celestine, orthorhombic, *Pnma*) to $SrCO_3$ (the mineral strontianite, orthorhombic, *Pmcn*) was studied on Wombat using the current cell. The purposes of the experiments were twofold: firstly to demonstrate the capability of the cell and secondly to make a preliminary investigation into the effect of pressure on the rate of a hydrothermal mineral replacement reaction. Celestine ($SrSO_4$), a common mineral mostly found in sedimentary rocks, is the main natural resource of strontium (Hanor, 2004). Celestine is commercially used to produce strontium carbonate ($SrCO_3$), from which other strontium chemicals for various applications are obtained (Castillejos *et al.*, 1996). The conversion from $SrSO_4$ to $SrCO_3$ is currently achieved by either the black ash process or the direct conversion process (Carrillo *et al.*, 1995). The black ash process involves high-temperature (>1223 K) reduction, hot-water leaching and finally precipitation; therefore it is a complex and energy-intensive process. The direct conversion process is simpler and consumes less energy, as the process converts $SrSO_4$ directly to $SrCO_3$ in a carbonate solution under hydrothermal conditions.

The conversion rate is dependent on various parameters, and the optimization of these parameters is vital for efficient processing. While the effects of temperature, particle size and solution chemistry (CO_3^{2-}/SO_4^{2-} ratio) on the conversion kinetics have been reported (Castillejos *et al.*, 1996; Suarez-Orduna *et al.*, 2004), the effect of pressure has yet to be investigated. Since pressure leaching is becoming an efficient and economic process in hydrometallurgy of some metals (Rubisov *et al.*, 2000; Provis *et al.*, 2003), it is interesting to see how an increase in pressure affects the rate of the conversion from $SrSO_4$ to $SrCO_3$. The ability to control temperature and pressure independently using the new cell is ideal for this purpose, because the temperature can be maintained constantly at different pressures, and neutron diffraction makes it practicable to monitor the conversion progress *in situ*. Additionally, the high neutron flux of the OPAL reactor at ANSTO allows the collection of high-quality data with adequate counting statistics in a relatively short time. This study involved fluid phases, which slightly increased the background, and hence we collected diffraction patterns every 15 min to balance the time resolution and adequate signal-to-noise ratio.

In the hydrothermal conversion from $SrSO_4$ to $SrCO_3$, natural millimetre-sized celestine crystals with a pale-blue color from the Sakoang deposit, Mitsijo district, Mahajang province, Madagascar (South Australian Museum Registration Number G21074), were used as starting materials. They were hand selected, ultrasonically cleaned, crushed and sieved. Grain sizes between 150 and 400 μm were used in this study. Analytical grade $NaCO_3$ (≥99.0%, Sigma–Aldrich) was used to prepare the $NaCO_3$ solution. Heavy water (D_2O, provided by ANSTO) instead of ordinary water (H_2O) was used as the solvent for solution preparation aiming to avoid high background from incoherent scattering of hydrogen atoms. In each experimental run, the molar ratio between anions CO_3^{2-} in the freshly prepared solution and SO_4^{2-} in the $SrSO_4$ sample was set to 4, so that the overall reaction can be kept far from equilibrium during the course of the conversion. Specifically, 2 g of $SrSO_4$ grains were reacted with 200 ml of 0.218 *M* Na_2CO_3 solution in all three experiments, which were conducted in closed-loop mode at constant temperature (473 K) and flow rate (5 ml min^{-1}) but with varying pressures, namely 14, 20 and 24 MPa.

The reaction progress was followed by recording *in situ* neutron diffraction patterns. The reaction extent y was calculated by the general formula

$$y = (Y_0 - Y_t)/(Y_0 - Y_e) \times 100\%, \quad (1)$$

where Y_t, Y_0 and Y_e are the mass fractions of the reactant crystals at an arbitrary reaction time t, initially ($t = 0$) and at equilibrium ($t = \infty$, in this case $Y_e = 0$), respectively. The mass fractions of involved phases were obtained from the Rietveld (1969) phase quantification method based on the diffraction data. The Rietveld least-square fittings were performed with the aid of the computer program *GSAS* (Larson & Von Dreele, 2004; Toby, 2001); structure models for least-squares fittings were obtained from the Inorganic Crystal Structure Database (Nos. 92608 for $SrSO_4$, 166088 for $SrCO_3$), and were originally sourced from Jacobsen *et al.* (1998) and Antao & Hassan (2009), respectively.

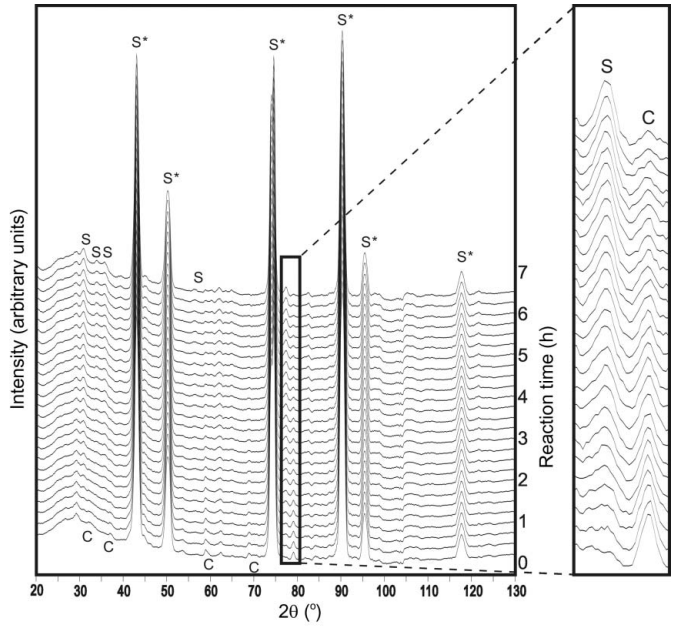

Figure 3
Neutron diffraction (λ = 1.54 Å) patterns of the conversion from $SrSO_4$ to $SrCO_3$ at 473 K and 14 MPa. C = $SrSO_4$, S = $SrCO_3$, S* = stainless steel.

The kinetics were then modeled by the Avrami equation (Xia *et al.*, 2007; Zhao *et al.*, 2009):

$$\ln\ln[1/(1-y)] = n\ln k + n\ln t. \quad (2)$$

From equation (2), the rate constants k and the time exponent n were extracted by plotting $\ln\ln[1/(1-y)]$ *versus* $\ln t$.

The *in situ* diffraction patterns for the conversion at 473 K and different pressures are similar in appearance, consisting of three observable phases (stainless steel, $SrSO_4$ and $SrCO_3$) and one nonlinear background arising from broad D_2O peaks mainly in the range below 50°. As an example, the diffraction patterns for the conversion at 14 MPa are shown in Fig. 3. The stainless steel peaks from the sample compartment tube and mesh basket are intense but remain constant throughout the reaction. In the 2θ range out of the stainless peak positions, *e.g.* the enlarged region in Fig. 3, it is clearly seen that the $SrCO_3$ diffraction peaks increase with time at the expense of those from $SrSO_4$. No other phase was observed as reaction

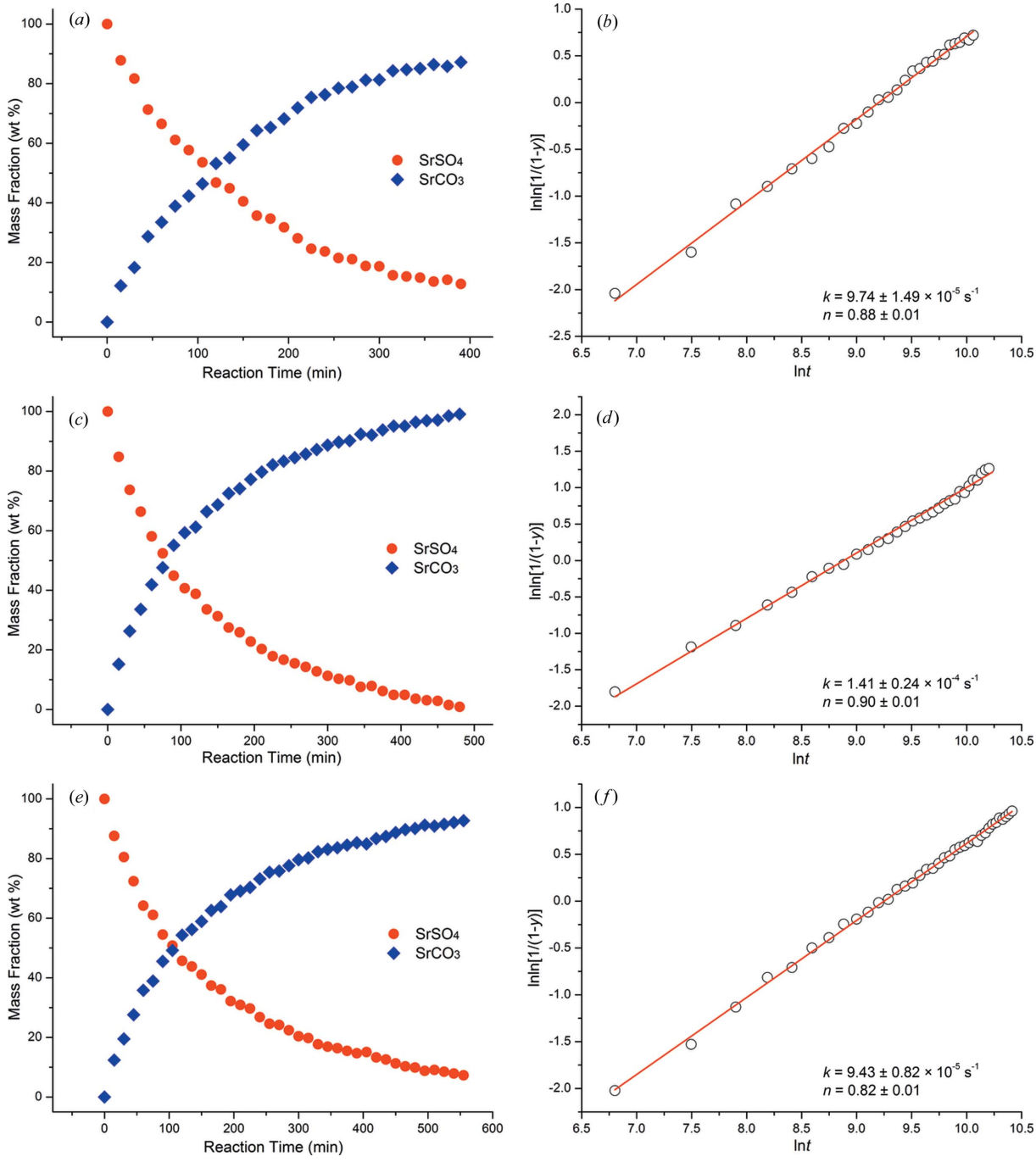

Figure 4
Plots of mass fractions as a function of reaction time and their corresponding Avrami plots for the calculation of rate constants k and time components n (value shown in the plots) during the conversion from $SrSO_4$ to $SrCO_3$ at 473 K and (*a*), (*b*) 14 MPa, (*c*), (*d*) 20 MPa and (*e*), (*f*) 24 MPa.

intermediate or by-product. These patterns undoubtedly indicate the progressive conversion from $SrSO_4$ directly to $SrCO_3$ without a crystalline intermediary phase.

The progress of the conversion is quantitatively seen in the plots of mass fraction evolution with reaction time (Figs. 4*a*, 4*c* and 4*e*), which reveal that, at 14 MPa, 87 wt% $SrSO_4$ was converted to $SrCO_3$ after 6.5 h, and at 20 and 24 MPa, a similar conversion extent required 4.75 and 7 h, respectively. The corresponding Avrami plots (Figs. 4*b*, 4*d* and 4*f*) give rate constants k and time exponents n; they are $k = 9.74\,(149) \times 10^{-5}\ s^{-1}$ and $n = 0.88\,(1)$ for the reaction at 14 MPa, $k = 1.41\,(24) \times 10^{-4}\ s^{-1}$ and $n = 0.90\,(1)$ for the reaction at 20 MPa, and $k = 9.43\,(82) \times 10^{-5}\ s^{-1}$ and $n = 0.82\,(1)$ for the reaction at 24 MPa. The time exponent n is an indication of reaction mechanism (Christian, 1965); hence the similar value of n for the three reactions means that the same reaction mechanism prevails in the conversion under different pressures (Christian, 1965). Previous studies have shown that the conversion is a topotaxially coupled dissolution–reprecipitation reaction mechanism (Suarez-Orduna *et al.*, 2004). Similar to the other mineral replacement reactions (Xia *et al.*, 2008; Janssen *et al.*, 2010; Putnis, 2009, 2002; Tenailleau *et al.*, 2006), the mechanism of the replacement from $SrSO_4$ to $SrCO_3$ is explained as follows. In contact with the carbonate solution, $SrSO_4$ dissolves from the surface, resulting in a local solution supersaturated with respect to $SrCO_3$ and causing the $SrCO_3$ to nucleate and grow on the surface of $SrSO_4$ (at or near $SrSO_4$ dissolution sites); the precipitation of $SrCO_3$ in turn brings the local solution back to the undersaturated state with respect to $SrSO_4$ and drives its further dissolution. In such a manner, the two half reactions finally become coupled such that the rate of $SrSO_4$ dissolution and $SrCO_3$ precipitation equalize, and this coupling is retained until the pseudomorphic conversion is complete; hence the product $SrCO_3$ retains the external dimension of the initial $SrSO_4$ as macroscopically observed. The mechanism can be illustrated by the following reaction equations: the dissolution of $SrSO_4$,

$$SrSO_4 \rightarrow Sr^{2+} + {SO_4}^{2-}, \tag{3}$$

coupled with local precipitation of $SrCO_3$ onto the grain boundary (the interface between $SrSO_4$ and $SrCO_3$),

$$Sr^{2+} + {CO_3}^{2-} \rightarrow SrCO_3. \tag{4}$$

The overall conversion can be written as

$$SrSO_4 + {CO_3}^{2-} \rightarrow SrCO_3 + {SO_4}^{2-}. \tag{5}$$

Because the temperature was kept at 473 K, the flow rate was set at 5 ml min^{-1} and the conversion mechanism is the same for the studied pressure range, it is meaningful to discuss the effect of pressure on the conversion rate, and it is the first time the effect of pressure on a couple dissolution reprecipitation reaction has been investigated. The kinetic data suggest that the reaction rate increases with increasing pressure from 14 to 20 MPa, and then decreases when the pressure further increases from 20 to 24 MPa. Therefore, an optimized pressure must exist in the range from 14 to 24 MPa for the rapid conversion from $SrSO_4$ to $SrCO_3$.

This nonlinear relationship between the conversion rate and the pressure further illustrates the complexity of interface-coupled dissolution–reprecipitation replacement reactions, as has been discussed in a recent work (Qian *et al.*, 2011). These reactions often occur in a non-intuitive manner, *e.g.* nonlinear dependence of reaction rate on temperature (Xia, Brugger, Chen *et al.*, 2009), formation of thermodynamically unexpected mineral phases (Xia, Brugger, Chen *et al.*, 2009; Qian *et al.*, 2011), unpreserved crystallographic orientation in spite of structural similarity between parent and daughter minerals (Qian *et al.*, 2011), the dependence of reaction kinetics on sample texture (Xia *et al.*, 2007), and so on.

Further work is clearly required to investigate the nonlinear effect of pressure on the conversion rate from $SrSO_4$ to $SrCO_3$. In particular, the reproducibility of the experimental results needs be tested, and the pressure dependence measured over a wide range and at higher pressure resolution. However, we note that a significant effect of pressure on interface-coupled dissolution–reprecipitation reactions is not unexpected. On one hand, elevated pressure can usually accelerate the rate of mineral dissolution, which is termed 'pressure solution', a common phenomenon occurring deep in the Earth's crust and one that has been believed to be the main mechanism responsible for rock deformation (Rutter, 1983; Baker *et al.*, 1980; Tada & Siever, 1986). Therefore, it is not surprising that the increase of pressure from 14 to 20 MPa increases the dissolution rate of $SrSO_4$ and hence the overall conversion rate. On the other hand, the conversion process is not a simple dissolution process, as it also involves a coupled precipitation process. The increase of pressure may further exert a kinetic factor on precipitation. The topotaxial conversion from $SrSO_4$ to $SrCO_3$ involves a contraction of 3.258 and 0.838 Å along the a and c axes and an expansion of 3.062 Å along the b axis of the orthorhombic unit cell (Suarez-Orduna *et al.*, 2004). The overall ~15.5% volume contraction is compensated by the formation of elongated pores randomly distributed parallel to the b axis (Suarez-Orduna *et al.*, 2004), which is in agreement with the contraction of the a and c axes. The important feature here is the induced stress along the b axis due to its expansion. Although the stress can be relieved by expanding excessive volume into the surrounding pores, the intentionally increased external pressure exerts further stress by pushing the newly formed $SrCO_3$ onto the $SrSO_4/SrCO_3$ grain boundary along the b axis. This squeezing effect would lead to limited space for $SrCO_3$ precipitation and therefore retard the overall conversion rate. Such twofold effects of pressure on dissolution and precipitation are competitive and may have a transition at around 20 MPa – below 20 MPa the pressure effect on the dissolution is more important, while above 20 MPa the pressure effect on precipitation dominates the overall conversion kinetics.

5. Conclusion

In summary, we have designed and constructed a versatile large-volume flow-through cell for *in situ* neutron diffraction studies of high-temperature and high-pressure hydrothermal

crystallizations, and have commissioned it on the HIPD beamline at ANSTO by investigating the effect of pressure on the hydrothermal pseudomorphic conversion from $SrSO_4$ to $SrCO_3$. The cell introduced several advantages compared with the previous cells in that temperature, pressure and flow rate can be independently controlled, providing a new avenue for studying hydrothermal crystallizations *in situ*, and possibly in real time. This kind of investigation will definitely deepen our understanding of the mechanisms and kinetics of hydrothermal crystallization processes by providing a clearer picture of these complex processes. One limitation of the cell is the intense stainless steel peaks arising from the sample compartment tubing and mesh container, which may be overcome by replacing them with a non-scattering Ti/Zr alloy (Sidhu *et al.*, 1956; Gray & Bailey, 2008); this modification will be tested in future experiments.

This work is financially supported by the Australian Research Council (grant No. DP1095069) and the Australian Institute of Nuclear Science and Engineering (AINSE). We thank Mr Jason Peak (Chemical Engineering Workshop at the University of Adelaide) for the construction of the cell and Dr Andrew Studer (HIPD beamline scientist) for assistance with instrumental setup.

References

Antao, S. M. & Hassan, I. (2009). *Can. Mineral.* **47**, 1245–1255.
Baker, P. A., Kastner, M., Byerlee, J. D. & Lockner, D. A. (1980). *Mar. Geol.* **38**, 185–203.
Brugger, J., Mcfadden, A., Lenehan, C. E., Etschmann, B., Xia, F., Zhao, J. & Pring, A. (2010). *Chimia*, **64**, 693–698.
Brugger, J., Pring, A., Reith, F., Ryan, C., Etschmann, B., Liu, W., O'Neill, B. & Ngothai, Y. (2010). *Radiat. Phys. Chem.* **79**, 151–161.
Carrillo, F. R., Uribe, P. & Castillejos, A. H. (1995). *Miner. Eng.* **8**, 495–509.
Castillejos, A. H., delaCruz, F. P. & Uribe, A. (1996). *Hydrometallurgy*, **40**, 207–222.
Christian, J. W. (1965). *The Theory of Transformations in Metals and Alloys.* Oxford: Pergamon Press.
Davis, M. E. & Lobo, R. F. (1992). *Chem. Mater.* **4**, 756–768.
Evans, J. S. O., Francis, R. J., O'Hare, D., Price, S. J., Clark, S. M., Flaherty, J., Gordon, J., Nield, A. & Tang, C. C. (1995). *Rev. Sci. Instrum.* **66**, 2442–2445.
Francis, R. J., O'Brien, S., Fogg, A. M., Halasyamani, P. S., O'Hare, D., Loiseau, T. & Ferey, G. (1999). *J. Am. Chem. Soc.* **121**, 1002–1015.
Francis, R. J. & O'Hare, D. (1998). *J. Chem. Soc. Dalton Trans.* **19**, 3133–3148.
Gray, E. M. & Bailey, I. F. (2008). *J. Neutron Res.* **16**, 127–132.
Hanor, J. S. (2004). *J. Sediment. Res.* **74**, 168–175.
Jacobsen, S. D., Smyth, J. R., Swope, R. J. & Downs, R. T. (1998). *Can. Mineral.* **36**, 1053–1060.
Janssen, A., Putnis, A., Geisler, T. & Putnis, C. V. (2010). *Mineral. Mag.* **74**, 633–644.
Larson, A. C. & Von Dreele, R. B. (2004). Report LAUR 86-748. Los Alamos National Laboratory, New Mexico, USA.
Lasaga, A. C. (1998). *Kinetic Theory in the Earth Sciences.* Princeton University Press.
Mesu, J. G., van der Eerden, A. M., de Groot, F. M. & Weckhuysen, B. M. (2005). *J. Phys. Chem. B*, **109**, 4042–4047.
Nagy, K. L. & Lasaga, A. C. (1992). *Geochim. Cosmochim. Acta*, **56**, 3093–3111.
Ok, K. M., O'Hare, D., Smith, R. I., Chowdhury, M. & Fikremariam, H. (2010). *Rev. Sci. Instrum.* **81**, 125107.
O'Neill, B., Tenailleau, C., Ngothai, Y., Studer, A., Brugger, J. & Pring, A. (2006). *Physica B*, **385–386**, 942–945.
Provis, J. L., van Deventer, J. S. J., Rademan, J. A. M. & Lorenzen, L. (2003). *Hydrometallurgy*, **70**, 83–99.
Putnis, A. (2002). *Mineral. Mag.* **66**, 689–708.
Putnis, A. (2009). *Rev. Mineral. Geochem.* **70**, 87–124.
Qian, G., Brugger, J., Skinner, W. M., Chen, G. R. & Pring, A. (2010). *Geochim. Cosmochim. Acta*, **74**, 5610–5630.
Qian, G., Xia, F., Brugger, J., Skinner, W. M., Bei, J., Chen, G. & Pring, A. (2011). *Am. Mineral.* **96**, 1878–1893.
Rietveld, H. M. (1969). *J. Appl. Cryst.* **2**, 65–71.
Rubisov, D. H., Krowinkel, J. M. & Papangelakis, V. G. (2000). *Hydrometallurgy*, **58**, 1–11.
Ruiz, M. C., Vera, M. V. & Padilla, R. (2011). *Hydrometallurgy*, **105**, 290–295.
Rutter, E. H. (1983). *J. Geol. Soc.* (*London*), **140**, 725–740.
Sidhu, S. S., Heaton, L. R., Zauberis, D. D. & Campos, F. P. (1956). *J. Appl. Phys.* **27**, 1040–1042.
Studer, A. J., Hagen, M. E. & Noakes, T. J. (2006). *Physica B*, **385–386**, 1013–1015.
Suarez-Orduna, R., Rendon-Angeles, J. C., Lopez-Cuevas, J. & Yanagisawa, K. (2004). *J. Phys. Condens. Matter*, **16**, S1331–S1344.
Tada, R. & Siever, R. (1986). *Geochim. Cosmochim. Acta*, **50**, 29–36.
Tenailleau, C., Pring, A., Etschmann, B., Brugger, J., Grguric, B. A. & Putnis, A. (2006). *Am. Mineral.* **91**, 706–709.
Toby, B. H. (2001). *J. Appl. Cryst.* **34**, 210–213.
Walton, R. I., Francis, R. J., Halasyamani, P. S., O'Hare, D., Smith, R. I., Done, R. & Humphreys, R. J. (1999). *Rev. Sci. Instrum.* **70**, 3391–3396.
Walton, R. I. & O'Hare, D. (2000). *Chem. Commun.* pp. 2283–2291.
Walton, R. I., Smith, R. I., Millange, F., Clark, I. J., Sinclair, D. C. & O'Hare, D. (2000). *Chem. Commun.* pp. 1267–1268.
Williams, G. R., Norquist, A. J. & O'Hare, D. (2006). *Chem. Mater.* **18**, 3801–3807.
Xia, F., Brugger, J., Chen, G. R., Ngothai, Y., O'Neill, B., Putnis, A. & Pring, A. (2009). *Geochim. Cosmochim. Acta*, **73**, 1945–1969.
Xia, F., Brugger, J., Ngothai, Y., O'Neill, B., Chen, G. & Pring, A. (2009). *Cryst. Growth Des.* **9**, 4902–4906.
Xia, F., O'Neill, B., Ngothai, Y., Peak, J., Tenailleau, C., Etschmann, B., Qian, G., Brugger, J., Studer, A., Olsen, S. & Pring, A. (2010). *J. Appl. Cryst.* **43**, 511–519.
Xia, F., Qian, G., Brugger, J., Studer, A., Olsen, S. & Pring, A. (2010). *Rev. Sci. Instrum.* **81**, 105107.
Xia, F., Zhou, J. W., Brugger, J., Ngothai, Y., O'Neill, B., Chen, G. R. & Pring, A. (2008). *Chem. Mater.* **20**, 2809–2817.
Xia, F., Zhou, J., Pring, A., Ngothai, Y., O'Neill, B., Brugger, J., Chen, G. & Colby, C. (2007). *React. Kinet. Catal. Lett.* **92**, 257–266.
Zhao, J., Brugger, J., Grundler, P. V., Xia, F., Chen, G. & Pring, A. (2009). *Am. Mineral.* **94**, 1541–1555.
Zhao, J., Xia, F., Pring, A., Brugger, J., Grundler, P. V. & Chen, G. (2010). *Miner. Eng.* **23**, 451–453.